



Atmospheric circulation and hydroclimate impacts of alternative warming scenarios for the Eocene

Henrik Carlson and Rodrigo Caballero

Department of Meteorology and Bolin Centre for Climate Research, Stockholm University, 106 91, Stockholm, Sweden

Correspondence to: Henrik Carlson (henrik@misu.su.se)

Received: 12 February 2017 – Discussion started: 21 February 2017

Revised: 22 June 2017 – Accepted: 12 July 2017 – Published: 18 August 2017

Abstract. Recent work in modelling the warm climates of the early Eocene shows that it is possible to obtain a reasonable global match between model surface temperature and proxy reconstructions, but only by using extremely high atmospheric CO₂ concentrations or more modest CO₂ levels complemented by a reduction in global cloud albedo. Understanding the mix of radiative forcing that gave rise to Eocene warmth has important implications for constraining Earth's climate sensitivity, but progress in this direction is hampered by the lack of direct proxy constraints on cloud properties. Here, we explore the potential for distinguishing among different radiative forcing scenarios via their impact on regional climate changes. We do this by comparing climate model simulations of two end-member scenarios: one in which the climate is warmed entirely by CO₂ (which we refer to as the greenhouse gas (GHG) scenario) and another in which it is warmed entirely by reduced cloud albedo (which we refer to as the “low CO₂–thin clouds” or LCTC scenario). The two simulations have an almost identical global-mean surface temperature and equator-to-pole temperature difference, but the LCTC scenario has ~11 % greater global-mean precipitation than the GHG scenario. The LCTC scenario also has cooler midlatitude continents and warmer oceans than the GHG scenario and a tropical climate which is significantly more El Niño-like. Extremely high warm-season temperatures in the subtropics are mitigated in the LCTC scenario, while cool-season temperatures are lower at all latitudes. These changes appear large enough to motivate further, more detailed study using other climate models and a more realistic set of modelling assumptions.

1 Introduction

The early Eocene (~50 Ma) was characterized by very warm surface temperatures compared with the present day (Huber, 2008; Pagani et al., 2014). Considerable progress has been made recently in reconciling proxy temperature reconstructions with climate model simulations of this period: models can now capture both the reconstructed global-mean and equator–pole temperature difference with much greater fidelity than before (Huber and Caballero, 2011; Lunt et al., 2012; Kiehl and Shields, 2013). A remaining problem is to understand what combination of radiative forcing and climate sensitivity gave rise to these very elevated temperatures in the first place (Caballero and Huber, 2013). While early Cenozoic CO₂ concentrations are understood to have been higher than modern ones (Royer, 2014), achieving a good match with reconstructed temperatures using CO₂ alone as the warming agent requires extremely high model CO₂ levels (Lunt et al., 2012), exceeding even the rather loose constraints imposed by the CO₂ proxies.

Non-CO₂ greenhouse gases such as methane and nitrous oxide may have contributed some of the warming (Beerling et al., 2011), but we lack suitable proxies to constrain their concentrations. Another hypothesis is that reduced aerosol loading during the Eocene could play an important role, particularly via its effect on cloud properties (Kump and Pollard, 2008; Kiehl and Shields, 2013). In a pre-industrial climate aerosol inventories are largely controlled by biological productivity (Andreae, 2007). In a very warm climate, it is possible that temperature limits could be exceeded over large areas of the tropics and subtropics (Huber, 2008) that would sharply limit primary production there, reducing emissions of aerosol precursors to the atmosphere. Further, increased ocean stratification could put further stress on ocean biota,

limiting the emission of sulfate precursors (Behrenfeld et al., 2006), while stomatal closure in an elevated CO₂ environment could reduce the emission of organic aerosol precursors from terrestrial plants (Acosta-Navarro et al., 2014). Reduced abundance of aerosols and cloud condensation nuclei is generally thought to lead to larger cloud droplets and reduced cloud albedo (Lohmann and Feichter, 2005). A global reduction in aerosol loading would thus lead to lower planetary albedo and a warmer climate. However, we again lack proxies to constrain paleo-aerosol abundances, and cloud–aerosol interactions themselves are still imperfectly understood (Stevens and Feingold, 2009), so this scenario remains highly speculative: given the current level of understanding, a substantial decrease in aerosol loading and cloud albedo during the Eocene can be neither confirmed nor ruled out with any degree of confidence. Nonetheless, the problem of disentangling the mix of radiative forcing agents that gave rise to Eocene warmth remains of crucial importance given its implications for climate sensitivity and thus predictions of future climate change (Caballero and Huber, 2013).

Here, we explore the potential for constraining the radiative forcing mix responsible for Eocene warmth *indirectly* – that is, without relying on direct proxies for aerosols or non-CO₂ greenhouse gases. Different combinations of forcing agents supporting the same global-mean surface temperature may leave different signatures in other climatological fields that are potentially detectable in the geological record. We focus specifically on the distinction between warming by greenhouse gases – which affect the longwave radiation – and warming by reduced cloud albedo, which affects solar radiation. We do this by comparing simulations of the Eocene climate warmed with respect to the present solely by increased CO₂ – which we refer to as the greenhouse gas (GHG) scenario – with simulations using modern pre-industrial CO₂ warmed solely by reduced cloud albedo, but with indistinguishable global-mean surface temperature. As in previous work (Kump and Pollard, 2008; Kiehl and Shields, 2013), we reduce cloud albedo by globally increasing the prescribed size of cloud droplets; we refer to these as the “low CO₂–thin clouds” (LCTC) scenario (because the clouds are optically thinner in the shortwave spectrum). We pay particular attention to differences in surface temperature patterns and to the hydrological cycle, which is known to respond differently to warming by longwave and shortwave forcing (O’Gorman et al., 2012). A similar discussion arises in the context of geo-engineering proposals to artificially increase Earth’s planetary albedo in order to offset some of the warming due to anthropogenic CO₂ emissions; it is well known that the resulting climate has a significantly different hydrological cycle compared with a climate subject to the same net radiative forcing but due to a more modest increase in CO₂ (McNutt et al., 2015).

Differences in surface temperature patterns and in hydrological regime could potentially be detectable in the terrestrial record, particularly in vegetation. However, it is not our

goal here to provide an exhaustive comparison between our simulations and the extant terrestrial proxy record. Given the broad-brush approach we take, employing a globally uniform increase in cloud droplet radius, it is unlikely that such a detailed comparison would be very meaningful in any case. Instead, we focus on quantifying the differences between the two climates and understanding the climate dynamical processes that lead to these differences, with the aim of assessing whether these differences are large and robust enough to warrant further, more detailed work in this direction.

Our modelling approach is further described in Sect. 2. Section 3 presents an overview of the climatology in the GHG simulation and its changes in the LCTC case. Section 4 discusses the global-mean change in precipitation and its relation to energetic constraints. Regional climate differences between the two simulations and their relation to circulation changes are discussed in Sect. 5. Finally, Sect. 6 summarizes our conclusions.

2 Methods

2.1 Model and simulations

We employ the Community Atmospheric Model 3.1 (CAM3) developed by the National Center for Atmospheric Research (NCAR) (Collins et al., 2006b) at T42 resolution coupled to the Community Land Model 2 (CLM2) and to a slab ocean with uniform 50 m depth. Ocean heat transport and seasonal heat storage are approximated through a prescribed seasonally varying energy convergence field (“q-flux”) derived from a fully coupled Eocene simulation run to equilibrium for a corresponding climate (Huber and Caballero, 2011). The model is configured with Eocene geography and land surface cover as described in Sewall et al. (2000). Simulation climatologies are computed from 30 years of monthly output obtained after the model has reached equilibrium.

We focus on two end-member simulations of the Eocene: a GHG run warmed only by increasing CO₂ and an extreme LCTC run warmed only by decreasing the planetary albedo. In the GHG simulation CO₂ is set to 4480 ppm and the effective cloud droplet radius takes its default value (8 μm over land and 14 μm over ocean). Various aspects of this simulation have been previously described in previous work (Caballero and Huber, 2010; Huber and Caballero, 2011; Caballero and Huber, 2013). In the LCTC simulation, CO₂ takes its pre-industrial value of 280 ppm, while effective cloud droplet radius is increased by multiplying the default values by a uniform factor of 2.5, yielding 20 μm over land and 35 μm over ocean. Note that this retains the difference between land and ocean values, differently from Kiehl and Shields (2013), who used a single effective cloud droplet radius globally. There is little knowledge about the actual aerosol concentration during the Eocene, but present-day observations in remote regions indicate that a land–sea differ-

ence in droplet size can be expected even in the absence of anthropogenic emissions (Bréon and Colzy, 2000).

These are very large and likely unrealistic droplet sizes, chosen simply because they lead to the same global-mean surface temperature as in the GHG run. In addition, cloud microphysics aside from the effective cloud droplet radius is unchanged, which unrealistically neglects cloud lifetime effects and imposes a further limitation on the interpretation of the results. Our intention is to compare two end-member states which maximise the difference between the two warming agents. Intermediate combinations of CO₂ and cloud albedo (e.g. Kiehl and Shields, 2013) will presumably have intermediate climate impacts; to test this hypothesis, we also conducted a third simulation where CO₂ is set to 1120 ppm and droplet radii are scaled by a factor of 1.6 and confirmed that the resulting climate differs from the GHG in a qualitatively similar way as described below for the extreme LCTC case, but with smaller overall amplitudes. In the interest of conciseness we focus here only on the end-member cases.

Comparison of the annual-mean surface temperature and precipitation fields in the GHG case (which are presented in the following section) with the corresponding fully coupled Eocene simulation of Huber and Caballero (2011) shows good agreement, with zonal-mean temperature and precipitation differences on the order of ~ 2 K and ~ 1 mm day⁻¹ respectively. As discussed in Huber and Caballero (2011), the coupled model reproduces the available proxy temperature reconstructions reasonably well, with no appreciable bias in either the global-mean temperature or the mean equator–pole temperature difference. As shown in Carmichael et al. (2016) (where this simulation is referred to as CCSM_H-16x), the precipitation field is also in broad agreement with a global compilation of precipitation proxies, albeit with some mismatches particularly in the Southern Hemisphere high latitudes. This provides confidence that the GHG simulation is a reasonable approximation to the Eocene climate at least in the annual mean. However, seasonal biases are larger, with a reduction in the annual temperature range in mid- to high latitudes of around 5 K in the GHG simulation compared to the full coupled model. This should be borne in mind when interpreting the climatologies below. These seasonal biases could possibly be corrected by suitably adjusting the q-flux and/or slab depth. Nonetheless, since our main focus in this paper is on the differences between two simulations using the same slab ocean configuration, we believe our results should be at least qualitatively robust to the details of the q-flux specification.

3 Climatologies

This section describes the main climatological features of the two simulations, to be further analysed and interpreted in subsequent sections.

Zonal- and annual-mean profiles of surface temperature and precipitation for the two simulations are presented in Fig. 1. Despite their very different radiative forcing agents, the two simulations have almost identical zonal-mean temperatures, differing at most by around 0.9 K. In the global mean, the LCTC simulation is cooler by 0.3 K than the GHG simulation. Precipitation, on the other hand, is significantly larger in the LCTC case, especially in the tropics and in the subtropical flanks of the major midlatitude precipitation zones.

As shown in Fig. 2b, however, regional differences in surface temperature are large. Land areas are cooler in the LCTC run by up to 5 K, particularly in subtropical regions with little cloud cover (Fig. 2e); the annual-mean climatology in the LCTC case is shown in Fig. S1 in the Supplement. Offsetting warming develops over the oceans, notably in twin horseshoe-shaped regions of the Pacific in both hemispheres. These temperature responses are accompanied by large changes in the low-level circulation (Fig. 2b). The LCTC case exhibits a cyclonic anomaly over the northern Pacific, with a similar but weaker response over the southern Pacific. The cyclonic anomaly acts to weaken the prevailing subtropical anticyclones seen in the GHG case (Fig. 2a). This is reminiscent of the weakening of the subtropical anticyclones seen in the transition from summer to winter in the modern day, which is also accompanied by a cooling of the continents relative to the oceans.

While global-mean temperature is very similar in the two simulations, global-mean precipitation is 3.8 mm day⁻¹ in the GHG simulation and 0.43 mm day⁻¹ or about 11 % higher in the LCTC case. This must be considered a substantial increase: Carmichael et al. (2016, their Figure 2c) show a robust linear scaling of precipitation with temperature of around 0.06 mm day⁻¹ K⁻¹, implying that a precipitation increase of this magnitude would require a CO₂-driven warming in excess of 7 K (comparable to that across the Paleocene–Eocene Thermal Maximum (PETM) hyperthermal event; see Pagani et al., 2014). For comparison, a present-day simulation using CAM3 (Collins et al., 2006a) has a global-mean temperature around 15 K cooler and precipitation around 0.9 mm day⁻¹ lower than the GHG simulation, in agreement with the scaling above.

As shown in Fig. 2d the spatial distribution of the precipitation change is highly non-uniform, with regional increases well in excess of 100 %. The greatest precipitation increase is concentrated in the central and eastern equatorial Pacific, partly offset by a large decrease in the western Pacific Warm Pool region. Precipitation also increases across large swaths of the subtropical to midlatitude Pacific and Atlantic oceans and adjacent land areas.

Cloud cover in the GHG simulation (Fig. 2e) shows broad-scale structures similar to the modern day, with abundant cloud cover over the Pacific Warm Pool and intertropical convergence zones (ITCZs) and over the midlatitude oceanic storm tracks and extensive stratocumulus decks in the eastern

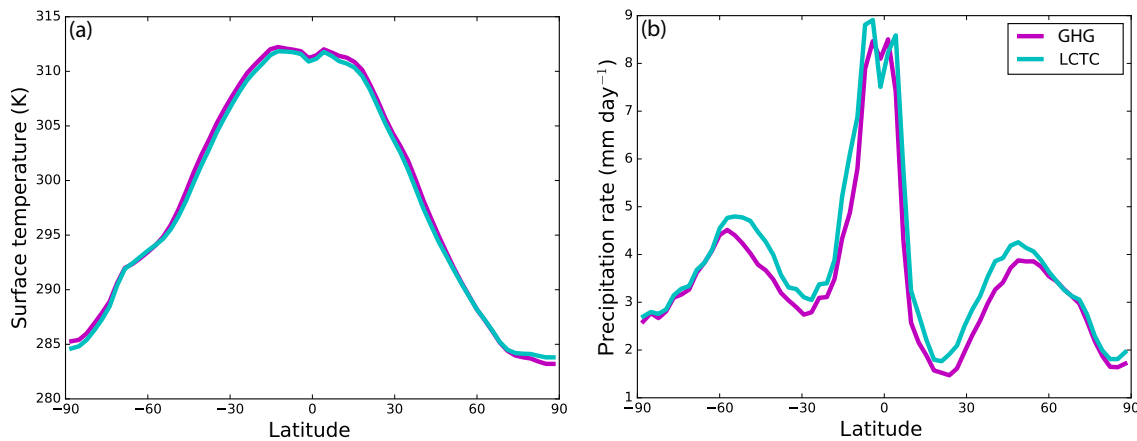


Figure 1. Annual- and zonal-mean surface temperature (a) and precipitation (b) in the GHG case (magenta) and LCTC case (cyan).

subtropical margins of the main ocean basins. Though our LCTC simulation only prescribes changes in cloud droplet size and CO_2 , the resulting dynamical and thermodynamical changes lead to changes also in cloud fraction (Fig. 2f). In particular, there is a substantial decrease in cloud fraction in the North Pacific subtropics – in the same region showing a large sea-surface temperature (SST) warming (Fig. 2b) – and increased cloud cover over southwestern North America, associated with increased precipitation there (Fig. 2d).

Figure 2g, h examine the atmospheric jets and storm tracks in the two simulations. As in the modern climate, zonal winds in the Northern Hemisphere of the GHG simulation are concentrated into separate jet streams spanning the Pacific and Atlantic basins; differently from modern times, the Pacific jet exhibits a marked meridional tilt. The Pacific jet's modern structure is well represented in modern-day simulations using CAM3 (Hurrell et al., 2006), so the jet's meridional tilt in our GHG simulation appears to be an intrinsic feature of this climate state, potentially related to its high CO_2 (Grise and Polvani, 2013) and to the structure of Asian orography, which lacks the modern Tibetan Plateau and instead presents a more continuous north–south obstacle with modest elevation (Brayshaw et al., 2009; Löfverström et al., 2016). The jets are associated with regions of enhanced eddy variability – storm tracks – which are approximately identified here by the sub-monthly eddy kinetic energy $\text{EKE} = (u'^2 + v'^2)/2$, where u and v are zonal and meridional components of the wind and primes denote sub-monthly deviations from monthly climatology. Lower-tropospheric jets and storm tracks are intimately connected via wave-mean flow interaction (Shaw et al., 2016). In the GHG run, the North Pacific storm track is further northward than observed in the modern climate (Shaw et al., 2016), consistent with the strong meridional tilt of the Pacific jet. In the LCTC case, however, the North Pacific jet and storm track show a marked equatorward shift, with enhanced winds and EKE in the subtropical basin and reductions further north. In the Southern Hemisphere the jet

and storm tracks are more zonally continuous, but a similar equatorward shift can be observed in the LCTC case. Along the equator, the LCTC case shows a low-level westerly wind anomaly in the western Pacific, consistent with a weakening of the Walker cell and an eastward shift in precipitation towards the central Pacific as noted above. There is also a marked reduction in EKE in the western equatorial Pacific, in the same region where precipitation decreases. Much of the sub-seasonal variability in the tropics is due to the Madden–Julian oscillation (MJO). As discussed elsewhere (Caballero and Huber, 2010; Arnold et al., 2014; Carlson and Caballero, 2016), warm climates show a strongly enhanced MJO in a range of climate models including the one used here. It is possible that the MJO is more muted in the LCTC simulation, perhaps because of changes in the Walker cell, but we do not investigate this issue further here.

Figure 3 compares the two simulations' annual and diurnal surface temperature ranges, which play an important role in determining both floral and faunal species ranges (Pearson and Dawson, 2003). Monthly-mean temperatures during the warmest month in the GHG simulation are above 320 K over large parts of the subtropical continents (Fig. 3a), potentially exceeding the survivability limits of vegetation there (Huber, 2008). These regions are cooler in the LCTC case (Fig. 3b) due to generally low cloud cover there – which limits the warming effect of thinner clouds – combined with the lower CO_2 . This LCTC cooling, though modest (generally around 3–5 K) could facilitate the survival of plants over the summer. Palynological evidence from northwestern South America (Jaramillo et al., 2006) indicates high floral biodiversity there, suggesting little environmental stress; however, this evidence comes from a near-equatorial region where both simulations show more moderate warm-month temperatures in addition to high precipitation. Floral reconstructions directly relevant to the extremely warm subtropical regions appear to be lacking at present. At higher latitudes, summer temperatures are somewhat warmer in the LCTC than the

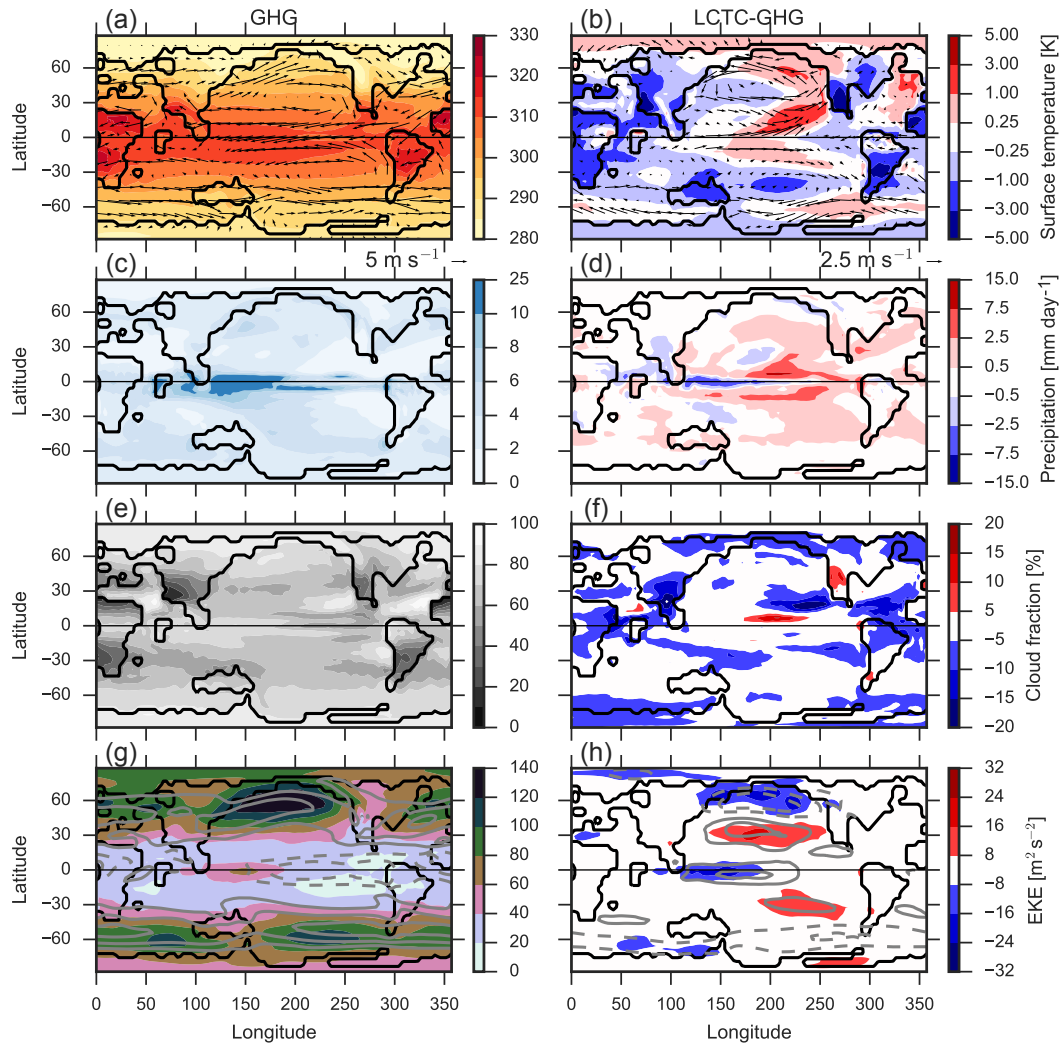


Figure 2. Annual-mean climatology in the GHG run (left column) and its change in the LCTC case (right column) of (a, b) surface temperature (shading) and 900 hPa wind (arrows), (c, d) precipitation, (e, f) cloud fraction, and (g, h) eddy kinetic energy (shading) and zonal wind at 700 hPa (contours; contour intervals 4 m s^{-1} in g and 2 m s^{-1} in h).

GHG case, presumably because high cloud cover there allows the warming effect of thinner clouds to dominate over the reduction in CO_2 .

Cold-month temperatures are above freezing everywhere in the GHG simulation except for parts of eastern Asia and North America (identified by white contours in Fig. 3c). In the LCTC simulation, cold-month temperatures are generally cooler, consistent with a weaker warming effect by thin clouds during winter when insolation is low. This leads to a moderate expansion of the regions experiencing sub-freezing winter temperatures, though importantly both the Arctic Ocean and Antarctica remain above freezing. There is substantial fossil evidence for subtropical, frost-intolerant flora and fauna surviving in western continental interiors and along the margins of the Arctic Ocean during the early Eocene (Markwick, 1998; Greenwood and Wing, 1995), and

both GHG and LCTC simulations are largely compatible with such evidence.

Lastly, we turn to the diurnal surface temperature range, estimated as the difference in monthly-mean maximum and minimum temperatures at each grid point (these quantities are not available in the model output over oceans, so only land values are shown in Fig. 3e, f). The annual-mean diurnal temperature range in the GHG simulation (Fig. 3e) is large over parts of the subtropical continents, particularly in western Asia and North America where it locally exceeds 16 K, consistent with low cloudiness in those regions. In the LCTC case, the diurnal temperature range is modestly larger over most continental regions; this enhancement in the LCTC case can be ascribed to greater daytime heating due to reduced cloud albedos and greater nighttime cooling due to reduced CO_2 . The enhancement is markedly stronger over subtropical

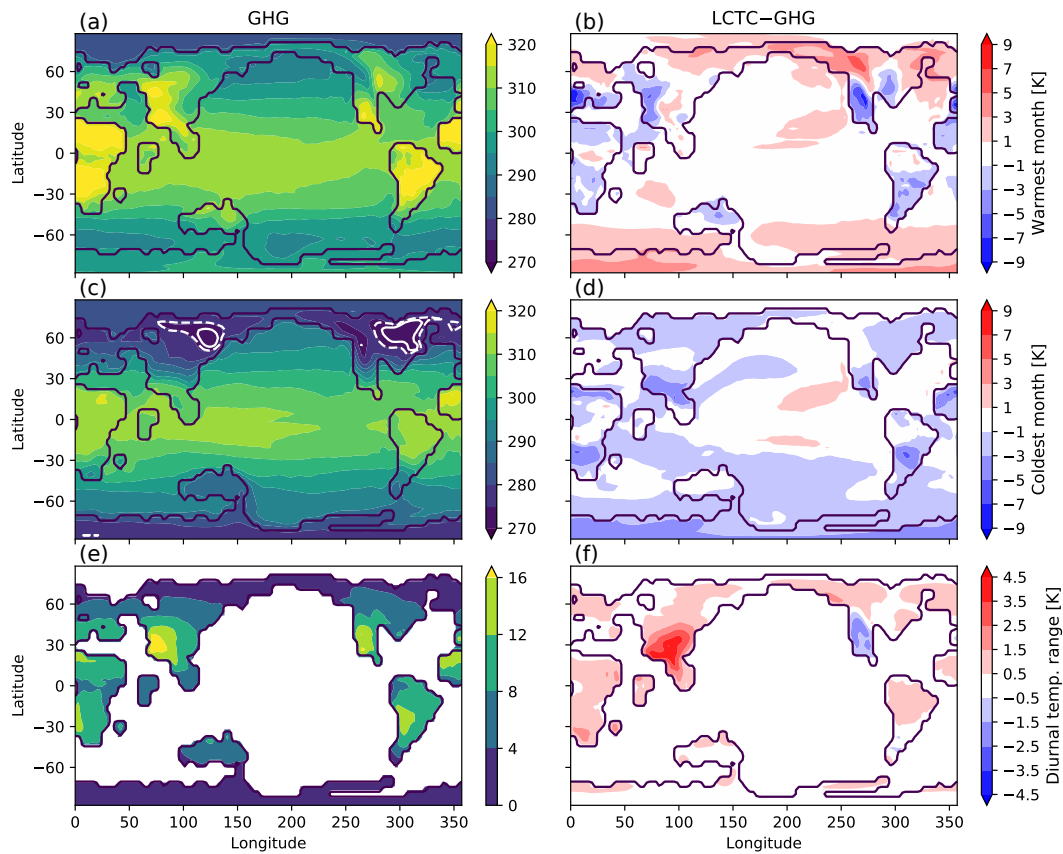


Figure 3. Monthly-mean surface temperature during the warmest month at each grid point in the GHG simulation (a) and its change in the LCTC simulation (b). (c, d) Same as in (a, b) but for the coldest month. (e) Annual-mean diurnal range in surface temperature, defined as the difference between daily maxima and minima, and (f) its change in the LCTC case. White lines in (c) indicate the 0°C contour in the GHG case (solid) and the LCTC case (dashed).

and midlatitude Asia, where it is up to 50 % greater than in the GHG case, which we ascribe to the substantial decrease in cloud cover in that region (Fig. 2f). Conversely, subtropical North America experiences a diurnal temperature range around 20 % smaller than in the GHG case, consistent with increased cloud cover there which overcompensates for the reduced cloud albedo.

4 Global-mean precipitation and energetic constraints

As noted above, global-mean precipitation in the LCTC case is around 11 % higher than in the GHG. A precipitation increase in response to a simultaneous drop in CO_2 and planetary albedo is consistent with simulations of geoengineering scenarios, where increased CO_2 and planetary albedo lead to lower precipitation (Bala et al., 2008). In this section we account for the global-mean precipitation change in our simulations from the perspective of energy budget constraints (O’Gorman et al., 2012).

Assuming steady state, the global-mean atmospheric energy budget can be written as

$$\text{SW}_{\text{TOA}} - \text{SW}_{\text{srf}} + \text{LW}_{\text{TOA}} - \text{LW}_{\text{srf}} - \text{LH} - \text{SH} = 0, \quad (1)$$

where SW and LW refer to shortwave and longwave radiation, with subscripts TOA and srf indicating top of the atmosphere and surface fluxes respectively, while LH and SH are surface latent and sensible heat fluxes respectively. All fluxes are taken to be positive downwards. Given the atmospheric steady-state assumption, $\text{LH} = -L_v P$, where P is global-mean precipitation and L_v the latent heat capacity. If the planet as a whole is also in steady state, then $\text{SW}_{\text{TOA}} + \text{LW}_{\text{TOA}} = 0$ and (Eq. 1) reduces to the surface energy budget.

$$\text{SW}_{\text{srf}} + \text{LW}_{\text{srf}} + \text{LH} + \text{SH} = 0 \quad (2)$$

For climates in planetary energy balance, like those studied here, the atmospheric and surface energy budgets are thus equivalent and provide alternative and complementary perspectives on the mechanisms controlling changes in precipitation (Allen and Ingram, 2002; Pierrehumbert, 2002). We examine both perspectives here.

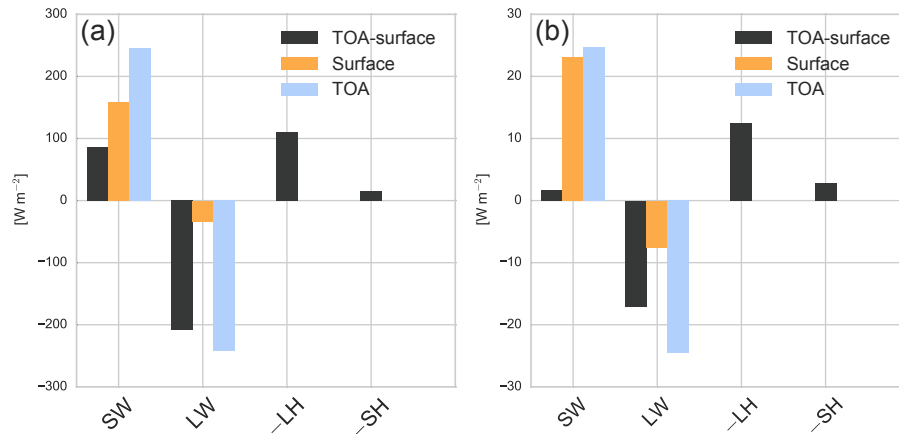


Figure 4. Terms in the global-mean atmospheric energy budget (Eq. 1) for (a) the GHG simulation and (b) change in the LCTC case (LCTC – GHG). The black bars are the atmospheric heating for both cases.

The terms in (Eq. 1) for the GHG case are shown in Fig. 4a. The LH is the largest component, but shortwave absorption ($SW_{TOA} - SW_{srf}$) also makes a large contribution as can be expected in this very warm and thus moist climate. Sensible heating makes a much smaller contribution. The heating is entirely balanced by net longwave cooling ($LW_{TOA} - LW_{srf}$). Changes when going to the LCTC case are shown in Fig. 4b. Net longwave cooling increases by about $17 W m^{-2}$ in the LCTC run. This increased cooling is a combination of clear-sky and cloud effects. In clear skies, lowering CO_2 while keeping temperature and humidity fixed yields stronger outgoing longwave radiation at the TOA (which increases atmospheric cooling) and weaker downward radiation at the surface (which decreases cooling). The former effect dominates the latter, however (Pendergrass and Hartmann, 2014), so the net result is increased cooling. The contribution of cloud effects can be estimated using the cloud radiative effect (CRE, difference between all-sky and clear-sky radiation). Net atmospheric longwave CRE – the difference between TOA and surface CRE – is about $13 W m^{-2}$ in the GHG case, implying that clouds have a net heating effect in the longwave. This heating drops to $7 W m^{-2}$ in the LCTC case, which means that cloud changes – including the general reduction in cloud cover seen in Fig. 2f as well as changes in cloud LW opacity due to increased effective drop radius – make a substantial contribution of around $6 W m^{-2}$ to the $17 W m^{-2}$ total increase in atmospheric cooling. Finally, Fig. 4b also shows that increased longwave cooling is balanced mostly by latent heating, with sensible heating and shortwave absorption playing minor roles. In summary, the atmospheric energy budget perspective indicates that precipitation increases in the LCTC run to compensate for increased longwave cooling due mostly to the clear-sky effect of reduced CO_2 , with a substantial contribution also from changes in cloud fraction and emissivity.

From the surface budget perspective (Eq. 2), Fig. 4b (noting the reversed sign convention) shows that increased shortwave heating of the surface in the LCTC case – due to the lower cloud albedo – is mainly compensated for through increased latent heat flux and also increased longwave surface cooling (due to reduced downwelling radiation, as noted above). From the surface perspective, then, precipitation increases in the LCTC case mostly to balance increased surface solar heating. This points to a rather different physical picture than the atmospheric perspective, in which shortwave fluxes play a negligible role. Given the equivalence of Eqs. (1) and (2), the two physical pictures must of course be consistent. A plausible hypothesis for how consistency is achieved runs as follows: atmospheric destabilization by radiative cooling due to reduced CO_2 accelerates convection, increasing rainfall and also mixing drier air down into the boundary layer; this drying increases evaporative demand at the surface, and the extra energy required to maintain surface temperature against evaporative cooling is supplied by increased solar absorption due to reduced cloud albedo. Fully reconciling the two perspectives in a causal, mechanistic way would require considerably more work going beyond the scope of this paper. However, some evidence supporting this hypothesis is shown in the following section.

5 Atmospheric circulation and regional climate response

While the energetic constraints discussed above help explain the global increase in precipitation in the LCTC case, they place no constraints on its spatial distribution, which is highly heterogeneous (Fig. 2d). These regional changes in precipitation are accompanied by pronounced changes in the surface temperature pattern (Fig. 2b) and the atmospheric general circulation (Fig. 2h). In this section we explore how these various changes are interrelated. To do this, it is useful

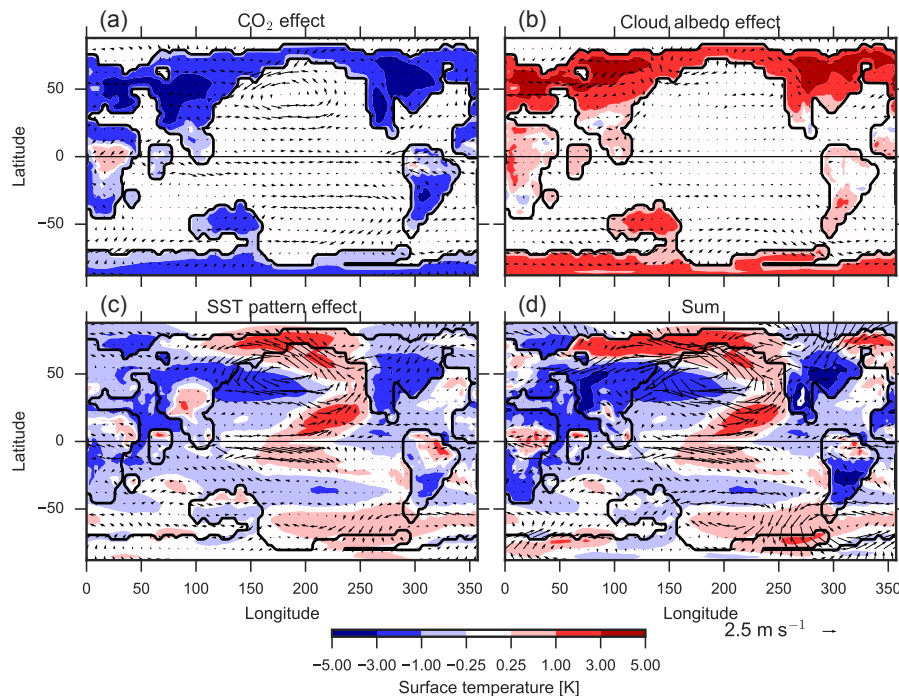


Figure 5. Change in annual-mean surface temperature (shading) and 900 hPa wind (arrows) between the GHG run and the fixed-SST simulation with (a) reduced CO₂, (b) reduced cloud albedo and (c) change in SST pattern, as well as (d) the sum of all changes.

to think of the transition from the GHG to the LCTC climate as if it occurred in three stages: first CO₂ is reduced instantaneously, producing a fast adjustment in the atmosphere and land before SST has time to change (Sherwood et al., 2015); then cloud albedo is instantaneously reduced, producing a further fast adjustment; and finally the SST slowly adjusts to its final equilibrium pattern. Circulation changes linked to the fast adjustments will condition the evolution of the SST pattern, which in turn will affect the circulation.

We make this conceptual picture quantitative by running three fixed-SST experiments. Two employ prescribed (seasonally varying) SST from the GHG run; one uses GHG values of cloud drop radius while CO₂ is reduced to 280 ppm, while the other uses GHG CO₂ and cloud drop radius increased by a factor of 2.5. The third run uses GHG values of CO₂ and cloud drop radius but prescribes the SST from the LCTC case. Comparing these fixed-SST simulations with the GHG run allows us to separately quantify the effect of changing CO₂, cloud albedo and SST pattern.

Figure 5 shows the surface temperature and low-level circulation responses in the three simulations. The sum of all changes (Fig. 5d) gives a reasonable match to the full response in the LCTC run (Fig. 2b), though with somewhat higher amplitude, suggesting that this linear decomposition is an adequate approximation. The direct response to reduced CO₂ (Fig. 5a) involves strong cooling of the extratropical continents and a basin-scale cyclonic anomaly over both the North and South Pacific, with westerly anomalies spanning

the tropics and lower midlatitudes and easterly anomalies further north. This is accompanied by an equatorward migration of the upper-level jets in both hemispheres, consistently with previous work (Grise and Polvani, 2013). Cooling of midlatitude land relative to the ocean accompanied by cyclonic anomalies over the ocean is reminiscent of the negative phase of the “cold ocean–warm land” pattern (Wallace et al., 1996). It is also consistent with the work of Molteni et al. (2011), who show cyclonic anomalies over the North Pacific in simulations with a permanently increased land–ocean temperature contrast and explore alternative dynamical scenarios to account for them.

The direct response to cloud albedo reduction (Fig. 5b) is a warming of the continents, particularly at high latitudes. This warming is highly seasonal, peaking in the summer, unlike the CO₂ response which is more even through the year. Somewhat surprisingly, the circulation response to continental warming is weak and not obviously anticyclonic except in the South Pacific. The reasons for this weak response are unclear; it is perhaps due to the seasonal and high-latitude nature of the warming, but we do not explore the issue further here.

Finally, the response to changing SST pattern (Fig. 5c) features a strong cyclonic anomaly over the North Pacific – where the SST anomaly is strongest – and a weaker cyclonic anomaly over the South Pacific. In the extratropics of both hemispheres, the circulation responses align with those induced by CO₂ alone and similarly yield an equatorward shift

in the lower-tropospheric jets. There is also a strong response in the tropics, in particular a westerly anomaly in the tropical west Pacific indicating a weakened Walker cell consistent with the substantial warm anomalies in the central Pacific.

Precipitation changes from the GHG for the three runs are presented in Fig. 6. The sum of all changes (Fig. 6d) again captures the change seen in the full LCTC case (Fig. 2d) reasonably well. Global-mean precipitation increases by 0.37 mm day^{-1} in response to CO_2 alone, by 0.05 mm day^{-1} in response to cloud albedo alone and decreases slightly in response to SST pattern. Thus, most of the 0.43 mm day^{-1} increase seen in the LCTC run is due to the direct effect of CO_2 . Reduced cloud albedo drives little change in precipitation by itself – instead, as discussed at the end of Sect. 4, it serves to close the surface energy balance, supplying surface solar heating to offset increased evaporative cooling. While CO_2 drives most of the global-mean precipitation change, its spatial pattern (Fig. 6a) shows anomalies concentrated in the eastern Pacific and over the Indo-Pacific warm pool, which is very different from that in the final state (Fig. 2d). Changes in SST pattern clearly play a major role in redistributing tropical precipitation into the central Pacific (Fig. 6c), consistent with warm SST anomalies there enhancing low-level convergence, as is evident in Fig. 5c.

Taken together, these results indicate a key role for the SST pattern in mediating the transition from the GHG to the LCTC climate state. So what gives rise to the SST anomaly? Some insight into this question is provided by the work of Vimont et al. (2001), who argue that a cyclonic circulation anomaly in the extratropical North Pacific will yield an SST “footprint” which has precisely the horseshoe structure we find here (compare their Fig. 1 with Fig. 2b). This happens because the anomalous surface winds affect surface energy fluxes. This interpretation is supported by Fig. 7, which shows the net surface energy flux change from the GHG to the fixed-SST low- CO_2 simulation. The pattern of ocean heating and cooling induced by these surface flux anomalies clearly aligns well with the SST anomaly (Fig. 5c). Note in particular that the surface energy flux anomaly will tend to warm the central Pacific relative to the rest of the equatorial zone, driving a shift in precipitation into the central Pacific.

A further important point highlighted by Fig. 5c is that the SST anomaly itself produces an extratropical circulation response that superposes constructively on the pre-existing CO_2 -induced cyclonic circulation anomaly. Given the generally weak atmospheric response to extratropical SST anomalies (Kushnir et al., 2002), it is most likely that this extratropical circulation response is driven from the tropics, in particular by a warm SST anomaly in the central Pacific which – as noted above – promotes large precipitation anomalies there, much like in an El Niño event. Such tropical heating anomalies are known to robustly induce cyclonic circulation anomalies in the extratropical North Pacific (Alexander et al., 2002). Furthermore, it is well known from both observations (Caballero, 2007) and model studies (Tandon et al.,

2013) that El Niño events and their associated tropical heating anomalies drive an equatorward shift in the extratropical jets and storm tracks, in agreement with what we find here (Fig. 2h).

In summary, the picture that emerges is that the direct effect of reduced CO_2 initially drives a basin-scale cyclonic circulation anomaly in each hemisphere of the Pacific Ocean; this circulation anomaly then drives SST anomalies which reinforce the initial response to CO_2 . The direct response to cloud albedo appears to play a minor role in driving regional climate changes. This picture points to an important limitation of our modelling approach, which uses a slab ocean model. With a dynamic ocean, the westerly wind anomalies along the equator (Fig. 7) would likely drive a deepening of the ocean thermocline in the eastern equatorial Pacific, shifting the mean climate towards a more El Niño-like state. This response and its global consequences are an important target for future work using a fully coupled modelling approach.

6 Conclusions

We have studied the differences in circulation and hydrological cycle resulting from two extreme scenarios by which Eocene simulations can attain surface temperatures compatible with proxy reconstructions: one by warming exclusively by increased CO_2 (the GHG case), the other by warming exclusively via reduced cloud albedo (the LCTC case). The two simulations have essentially identical zonal-mean surface temperature, but the LCTC case has significantly higher precipitation. Analysis of the global-mean energy budget (Sect. 4) suggests that the increased precipitation can be viewed as resulting from greater radiative cooling of the atmosphere in the LCTC case due to its lower CO_2 . The spatial distribution of the precipitation increase is highly heterogeneous and is concentrated largely in the central equatorial Pacific and in the lower midlatitudes. The midlatitude continents cool in the LCTC simulation, with compensating warming of the oceans in horseshoe-shaped patterns in both hemispheres of the Pacific. There are also major changes to the atmospheric circulation, with basin-scale cyclonic anomalies appearing in both hemispheres of the Pacific associated with equatorward shifts of the storm tracks, and a strong weakening of the Walker cell in the tropics.

More detailed analysis (Sect. 5) suggests that these various anomalies are dynamically interrelated. Lower CO_2 in the LCTC case leads to continental cooling, which in turn generates cyclonic circulation anomalies over the Pacific. We propose that these cyclonic anomalies in turn leave a horseshoe shaped footprint on SSTs via their effect on surface turbulent fluxes (Vimont et al., 2001). This footprint reaches into the central tropical Pacific and promotes increased convection there which, much as in a modern El Niño event, affects the extratropical circulation and enhances the pre-existing cyclonic anomalies. This self-reinforcing mechanism leads

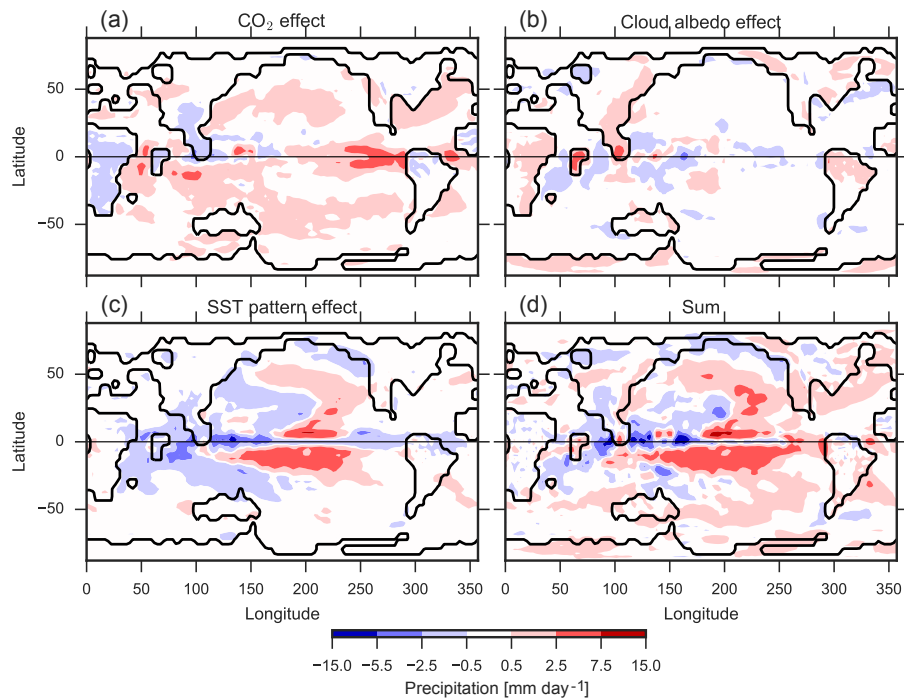


Figure 6. As in Fig. 5 but for annual-mean precipitation.

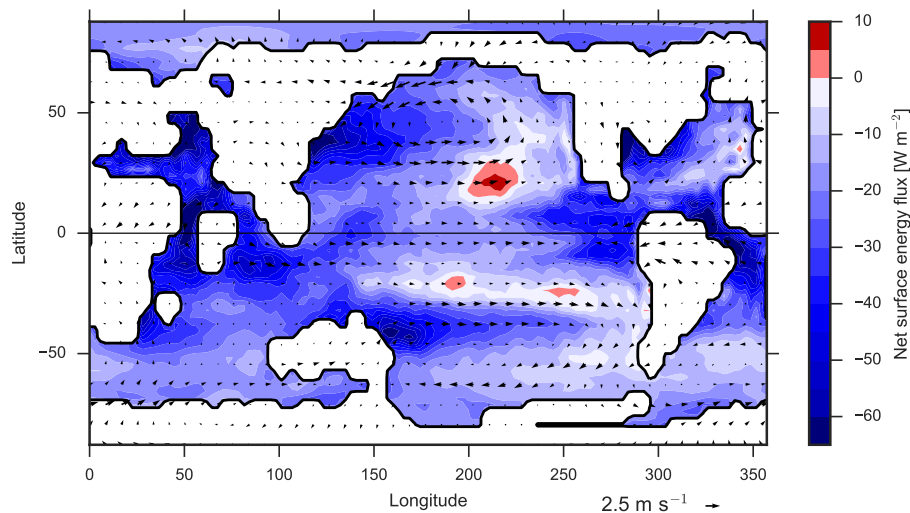


Figure 7. Change in annual-mean net surface energy flux (shading, defined positive downwards) and 900 hPa wind (arrows) between the GHG run and the fixed-SST run with reduced CO_2 .

to the pronounced regional climate anomalies noted above, which may also affect adjacent land areas.

Our work is intended as an initial exploration, and much work remains to be done to remove the limitations imposed by our choice of a relatively simplified modelling approach. A key limitation is our use of a slab ocean. As noted in Sect. 5, the ocean will dynamically respond to the westerly surface stress anomalies along the equator (Vimont et al., 2001), possibly leading to a climate state with a perma-

nently reduced tropical thermocline tilt and a more El Niño-like climate. If this were the case, the ocean dynamical response would in fact further strengthen the tropical anomalies found here, which already resemble an El Niño-like response. Another important caveat is that circulation responses to changes in radiative forcing – and their associated regional climate changes – are sensitive to biases in the unperturbed state (Shepherd, 2014). For example, if the Pacific jet were more zonally oriented in reality than in our

GHG Eocene simulation (Fig. 2g), its response in the LCTC scenario could be quite different. A further limitation of our approach is the specification of a uniformly increased cloud drop radius, leaving other aspects of cloud microphysics untouched. This is highly unrealistic in several ways: there is no particular reason to expect that different cloud types would respond in the same way to reduced aerosol loading; moreover, larger cloud drops are expected to coalesce more readily and thus reduce cloud lifetimes, potentially leading to reductions in cloud cover which would be different for different cloud types. In addition, all the above effects would depend on the precise nature and composition of natural aerosol in the Eocene, which remains essentially unknown. Different hypotheses for aerosol composition and cloud microphysics could lead to very different spatial structures of the resulting radiative forcing, with potentially large impacts on the circulation and regional climates.

Despite these important caveats, we conclude that differences in the radiative forcing agent driving Eocene warmth could at least in principle lead to large differences in regional climates leaving potentially detectable traces in the geological record. We have explored here two end-member scenarios, one with very high CO₂ (higher than suggested by current CO₂ proxy reconstructions) and another with pre-industrial CO₂ (which is almost certainly lower than in the Eocene). A more realistic scenario would involve some intermediate mix of warming by CO₂ and by cloud effects (Kiehl and Shields, 2013), which would be expected to yield smaller climate differences than those found here. However, given the large uncertainties discussed above, it remains possible that even an intermediate mix of warming agents could lead to responses as large or larger than those in our study. Future work with a range of models including more complete representations of ocean dynamics and cloud–aerosol interactions is required to settle this question.

Data availability. The source code for the Community Atmospheric Model 3.1 can be downloaded from <http://www.cesm.ucar.edu/models/atm-cam/download/>.

The Supplement related to this article is available online at <https://doi.org/10.5194/cp-13-1037-2017-supplement>.

Competing interests. The authors declare that they have no conflict of interest.

Acknowledgements. We thank Qiang Fu, Jack Scheff and Johan Nilsson for useful discussion and comments. We also thank two anonymous reviewers for constructive comments and suggestions. The Swedish National Infrastructure for Computing

(SNIC) at the National Supercomputing Centre (NSC), Linköping University, provided the high performance computing resources to perform the simulations.

Edited by: Arne Winguth

Reviewed by: two anonymous referees

References

- Acosta-Navarro, J. C., Smolander, S., Struthers, H., Zorita, E., Ekman, A. M., Kaplan, J., Guenther, A., Arneth, A., and Riipinen, I.: Global emissions of terpenoid VOCs from terrestrial vegetation in the last millennium, *J. Geophys. Res.-Ocean.*, 119, 6867–6885, 2014.
- Alexander, M. A., Bladé, I., Newman, M., Lanzante, J. R., Lau, N.-C., and Scott, J. D.: The atmospheric bridge: The influence of ENSO teleconnections on air–sea interaction over the global oceans, *J. Clim.*, 15, 2205–2231, 2002.
- Allen, M. R. and Ingram, W. J.: Constraints on future changes in climate and the hydrologic cycle, *Nature*, 419, 224–232, 2002.
- Andreae, M. O.: *ATMOSPHERE: Aerosols Before Pollution*, Science, 315, 50–51, 2007.
- Arnold, N. P., Branson, M., Burt, M. A., Abbot, D. S., Kuang, Z., Randall, D. A., and Tziperman, E.: Effects of explicit atmospheric convection at high CO₂, *P. Natl. Acad. Sci. USA*, 111, 10943–10948, 2014.
- Bala, G., Duffy, P., and Taylor, K.: Impact of geoengineering schemes on the global hydrological cycle, *P. Natl. Acad. Sci. USA*, 105, 7664–7669, 2008.
- Beerling, D. J., Fox, A., Stevenson, D. S., and Valdes, P. J.: Enhanced chemistry–climate feedbacks in past greenhouse worlds, *P. Natl. Acad. Sci. USA*, 108, 9770–9775, 2011.
- Behrenfeld, M. J., O’Malley, R. T., Siegel, D. A., McClain, C. R., Sarmiento, J. L., Feldman, G. C., Milligan, A. J., Falkowski, P. G., Letelier, R. M., and Boss, E. S.: Climate-driven trends in contemporary ocean productivity, *Nature*, 444, 752–755, 2006.
- Brayshaw, D. J., Hoskins, B., and Blackburn, M.: The basic ingredients of the North Atlantic storm track, Part I: Land–sea contrast and orography, *J. Atmos. Sci.*, 66, 2539–2558, 2009.
- Bréon, F.-M. and Colzy, S.: Global distribution of cloud droplet effective radius from POLDER polarization measurements, *Geophys. Res. Lett.*, 27, 4065–4068, 2000.
- Caballero, R.: Role of eddies in the interannual variability of Hadley cell strength, *Geophys. Res. Lett.*, 34, L22705, <https://doi.org/10.1029/2007GL030971>, 2007.
- Caballero, R. and Huber, M.: Spontaneous transition to superrotation in warm climates simulated by CAM3, *Geophys. Res. Lett.*, 37, L11701, <https://doi.org/10.1029/2010GL043468>, 2010.
- Caballero, R. and Huber, M.: State-dependent climate sensitivity in past warm climates and its implications for future climate projections, *P. Natl. Acad. Sci. USA*, 110, 14162–14167, <https://doi.org/10.1073/pnas.1303365110>, 2013.
- Carlson, H. and Caballero, R.: Enhanced MJO and transition to superrotation in warm climates, *J. Adv. Model. Earth Syst.*, 8, 304–318, 2016.
- Carmichael, M. J., Lunt, D. J., Huber, M., Heinemann, M., Kiehl, J., LeGrande, A., Loftson, C. A., Roberts, C. D., Sahoo, N., Shields, C., Valdes, P. J., Winguth, A., Winguth, C., and Pancost, R. D.: A model–model and data–model comparison for

- the early Eocene hydrological cycle, *Clim. Past*, 12, 455–481, <https://doi.org/10.5194/cp-12-455-2016>, 2016.
- Collins, W., Bitz, C., Blackmon, M., Bonan, G., Bretherton, C., Carton, J., Chang, P., Doney, S., Hack, J., Henderson, T. B., Kiehl, J. T., Large, W. G., McKenna, D. S., Santer, B. D., and Smith, R. D.: The Community Climate System Model Version 3 (CCSM3), *J. Clim.*, 19, 2122–2143, 2006a.
- Collins, W. D., Rasch, P. J., Boville, B. A., Hack, J. J., McCaa, J. R., Williamson, D. L., Briegleb, B. P., Bitz, C. M., Lin, S.-J., and Zhang, M.: The Formulation and Atmospheric Simulation of the Community Atmosphere Model Version 3 (CAM3), *J. Clim.*, 19, 2144–2161, <https://doi.org/10.1175/JCLI3760.1>, 2006b.
- Greenwood, D. R. and Wing, S. L.: Eocene continental climates and latitudinal temperature gradients, *Geology*, 23, 1044–1048, 1995.
- Grise, K. M. and Polvani, L. M.: Is climate sensitivity related to dynamical sensitivity? A Southern Hemisphere perspective, *Geophys. Res. Lett.*, 41, 534–540, <https://doi.org/10.1002/2013GL058466>, 2013.
- Huber, M.: CLIMATE CHANGE: A Hotter Greenhouse?, *Science*, 321, 353–354, <https://doi.org/10.1126/science.1161170>, 2008.
- Huber, M. and Caballero, R.: The early Eocene equable climate problem revisited, *Clim. Past*, 7, 603–633, <https://doi.org/10.5194/cp-7-603-2011>, 2011.
- Hurrell, J. W., Hack, J. J., Phillips, A. S., Caron, J., and Yin, J.: The dynamical simulation of the Community Atmosphere Model version 3 (CAM3), *J. Clim.*, 19, 2162–2183, 2006.
- Jaramillo, C., Rueda, M. J., and Mora, G.: Cenozoic plant diversity in the Neotropics, *Science*, 311, 1893–1896, 2006.
- Kiehl, J. T. and Shields, C. A.: Sensitivity of the Palaeocene-Eocene Thermal Maximum climate to cloud properties, *Philos. T. R. Soc. A*, 371, 20130093, <https://doi.org/10.1098/rsta.2013.0093>, 2013.
- Kump, L. R. and Pollard, D.: Amplification of Cretaceous Warmth by Biological Cloud Feedbacks, *Science*, 320, 195, <https://doi.org/10.1126/science.1153883>, 2008.
- Kushnir, Y., Robinson, W., Bladé, I., Hall, N., Peng, S., and Sutton, R.: Atmospheric GCM response to extratropical SST anomalies: Synthesis and evaluation, *J. Clim.*, 15, 2233–2256, 2002.
- Löfverström, M., Caballero, R., Nilsson, J., and Messori, G.: Stationary wave reflection as a mechanism for zonalising the Atlantic winter jet at the LGM, *J. Atmos. Sci.*, 73, 3329–3342, 2016.
- Lohmann, U. and Feichter, J.: Global indirect aerosol effects: a review, *Atmos. Chem. Phys.*, 5, 715–737, <https://doi.org/10.5194/acp-5-715-2005>, 2005.
- Lunt, D. J., Dunkley Jones, T., Heinemann, M., Huber, M., LeGrande, A., Winguth, A., Loptson, C., Marotzke, J., Roberts, C. D., Tindall, J., Valdes, P., and Winguth, C.: A model-data comparison for a multi-model ensemble of early Eocene atmosphere–ocean simulations: EoMIP, *Clim. Past*, 8, 1717–1736, <https://doi.org/10.5194/cp-8-1717-2012>, 2012.
- Markwick, P. J.: Fossil crocodylians as indicators of Late Cretaceous and Cenozoic climates: implications for using palaeontological data in reconstructing palaeoclimate, *Palaeogeogr. Palaeoclimatol.*, 137, 205–271, 1998.
- McNutt, M. K., Abdalati, W., Caldeira, K. et al.: *Climate Intervention: Reflecting Sunlight to Cool Earth*, National Academy of Sciences, Washington, DC, USA, 2015.
- Molteni, F., King, M. P., Kucharski, F., and Straus, D. M.: Planetary-scale variability in the northern winter and the impact of land–sea thermal contrast, *Clim. Dynam.*, 37, 151–170, 2011.
- O’Gorman, P. A., Allan, R. P., Byrne, M. P., and Previdi, M.: Energetic constraints on precipitation under climate change, *Surv. Geophys.*, 33, 585–608, 2012.
- Pagani, M., Huber, M., and Sageman, B.: Greenhouse climates, in: *Treatise on Geochemistry*, edited by: Holland, H. and Turekian, K., Elsevier, Oxford, 2nd Edn., 281–304, 2014.
- Pearson, R. G. and Dawson, T. P.: Predicting the impacts of climate change on the distribution of species: are bioclimate envelope models useful?, *Glob. Ecol. Biogeog.*, 12, 361–371, 2003.
- Pendergrass, A. G. and Hartmann, D. L.: The Atmospheric Energy Constraint on Global-Mean Precipitation Change, *J. Clim.*, 27, 757–768, 2014.
- Pierrehumbert, R. T.: The hydrologic cycle in deep-time climate problems, *Nature*, 419, 191–198, <https://doi.org/10.1038/nature01088>, 2002.
- Royer, D.: Atmospheric CO₂ and O₂ during the Phanerozoic: Tools, patterns, and impacts, in: *Treatise on Geochemistry*, edited by: Holland, H. and Turekian, K., 251–267, Elsevier, 2nd Edn., 2014.
- Sewall, J. O., Sloan, L. C., Huber, M., and Wing, S.: Climate sensitivity to changes in land surface characteristics, *Glob. Planet. Change*, 26, 445–465, 2000.
- Shaw, T. A., Baldwin, M., Barnes, E. A., Caballero, R., Garfinkel, C. I., Hwang, Y. T., Li, C., O’Gorman, P. A., Riviere, G., Simpson, I. R., and Voigt, A.: Storm track processes and the opposing influences of climate change, *Nat. Geosci.*, 9, 656–664, <https://doi.org/10.1038/ngeo2783>, 2016.
- Shepherd, T. G.: Atmospheric circulation as a source of uncertainty in climate change projections, *Nat. Geosci.*, 7, 703–708, 2014.
- Sherwood, S. C., Bony, S., Boucher, O., Bretherton, C., Forster, P. M., Gregory, J. M., and Stevens, B.: Adjustments in the forcing–feedback framework for understanding climate change, *Bull. Am. Meteorol. Soc.*, 96, 217–228, 2015.
- Stevens, B. and Feingold, G.: Untangling aerosol effects on clouds and precipitation in a buffered system, *Nature*, 461, 607–613, 2009.
- Tandon, N. F., Gerber, E. P., Sobel, A. H., and Polvani, L. M.: Understanding Hadley cell expansion versus contraction: Insights from simplified models and implications for recent observations, *J. Clim.*, 26, 4304–4321, 2013.
- Vimont, D., Battisti, D., and Hirst, A.: Footprinting: A seasonal connection between the tropics and mid-latitudes, *Geophys. Res. Lett.*, 28, 3923–3926, 2001.
- Wallace, J. M., Zhang, Y., and Bajuk, L.: Interpretation of interdecadal trends in Northern Hemisphere surface air temperature, *J. Clim.*, 9, 249–259, 1996.